arXiv:1510.04751v1 [astro-ph.GA] 16 Oct 2015

Si IV Column Densities Predicted from Non-Equilibrium Ionization Simulations of Turbulent Mixing Layers and High-Velocity Clouds

Kyujin Kwak[1], Robin L. Shelton[2], and David B. Henley[2]

[1]*School of Natural Science, Ulsan National Institute of Science Institute (UNIST), 50 UNIST-gil, Ulju-gun, Ulsan, 44919, Republic of Korea*

kkwak@unist.ac.kr

[2]*Department of Physics and Astronomy, University of Georgia, Athens, GA 30602*

rls@physast.uga.edu, dbh@physast.uga.edu

ABSTRACT

We present predictions of the Si IV ions in turbulent mixing layers (TMLs) between hot and cool gas and in cool high velocity clouds (HVCs) that travel through a hot halo, complementing the C IV, N V, and O VI predictions in Kwak & Shelton (2010), Kwak et al. (2011), and Henley et al. (2012). We find that the Si IV ions are most abundant in regions where the hot and cool gases first begin to mix or where the mixed gas has cooled significantly. The predicted column densities of high velocity Si IV and the predicted ratios of Si IV to C IV and O VI found on individual sightlines in our HVC simulations are in good agreement with observations of high velocity gas. Low velocity Si IV is also seen in the simulations, as a result of decelerated gas in the case of the HVC simulations and when looking along directions that pass perpendicular to the direction of motion in the TML simulations. The ratios of low velocity Si IV to C IV and O VI in the TML simulations are in good agreement with those recorded for Milky Way halo gas, while the ratio of Si IV to O VI from the decelerated gas in the HVC simulations is lower than that observed at normal velocity in the Milky Way halo. We attribute the shortfall of normal velocity Si IV to not having modeled the effects of photoionization and, following Henley et al. (2012), consider a composite model that includes decelerated HVC gas, supernova remnants, galactic fountain gas, and the effect of photoionization.

Subject headings: Galaxy: halo — Hydrodynamics — ISM: clouds — Methods: numerical — Ultraviolet: ISM

1. Introduction

Studies of the absorption lines in the ultraviolet (UV) spectra of early type stars and active galactic nuclei (AGNs) have found large numbers of high ions, such as Si IV, C IV, N V, and O VI in the Milky Way's disk (Jenkins 1978a,b; Cowie et al. 1981; Savage & Massa 1987; Savage et al. 2001a; Bowen et al. 2008) and halo (Sembach & Savage 1992; Savage & Sembach 1994; Sembach et al. 1997; Savage et al. 1997, 2001b; Sterling et al. 2002; Zsargó et al. 2003; Savage et al. 2003; Ganguly et al. 2005, 2006; Savage & Wakker 2009; Wakker et al. 2012). The observations also reveal a population of high velocity ($|v_{LSR}| \gtrsim 90$ km s^{-1}) high ions (Sembach et al. 2003; Fox et al. 2004, 2005, 2010; Collins et al. 2004, 2005, 2007; Ganguly et al. 2005; Shull et al. 2011). Some of these high-velocity high ions are observed along the same sightlines where H I high velocity clouds (HVCs) are observed, while others appear where H I HVCs have not been detected.

Transition temperature gas of $(0.5 - 10) \times 10^5$ K generally contains some high ions, but some Si IV and C IV can also exist at lower temperatures if sufficient ionizing radiation is incident upon the gas. Although gas of this temperature is unstable due to its large radiative cooling rate, it may come from the interaction and/or transition between hotter ($T > 10^6$ K) and cooler ($T < 10^4$ K) gases that are stable for longer periods of time.

In previous studies, we examined the mixing between cool and hot gases. In the first study (Kwak & Shelton 2010, hereafter KS10), turbulent mixing of cool and hot gas that slide past each other was simulated in 2D planar (Cartesian) coordinates. Hereafter, we call this set of simulations 'TML' (turbulent mixing layer) simulations. In the second study (Kwak et al. 2011, hereafter KHS11), we simulated cool spherical clouds falling through hot ambient gas in 2D cylindrical coordinates (such simulations are called 'HVC' simulations in this paper). In both sets of simulations, carried out with the FLASH hydrodynamics code (Fryxell et al. 2000), turbulent mixing is caused by shear instabilities that are instigated by the velocity difference between cool and hot gas. High ions are abundant in the resulting mixed gas. Our modeling included the effect of radiative cooling, assuming collisional ionization equilibrium (CIE) cooling rates. We also modeled the ionization states of carbon, nitrogen, and oxygen in the non-equilibrium fashion (i.e., the populations in all the ionization states of these elements were updated at each hydrodynamic time step). Note that our TML and HVC simulations are only different in their geometries (planar in a 2D domain versus round in a cylindrically symmetric domain) while their modeling includes the same physical processes.

In KS10 and KHS11, we also compared our predictions of the column densities of C IV, N V, and O VI (hereafter, N(C IV), N(N V), and N(O VI), respectively) with the observed column densities of these ions in the Galactic halo (both low and high velocity ions) and

predictions from other models and found that using reasonable choices of model parameters, our model predictions are generally in good agreement with observations. Furthermore, in our more recent study (Henley et al. 2012, hereafter HKS12), we estimated the amount of low-velocity C IV, N V, and O VI predicted from the same set of simulations as KHS11. These low-velocity ions exist in the decelerated mixed material and we found that our model clouds could provide a significant fraction of the low-velocity O VI that is observed in the halo. However, the quantity of low-velocity C IV is not large enough to explain a significant fraction of the low-velocity C IV ions observed in the halo. Thus, HKS12 suggested that some of the low-velocity C IV is produced via photoionization, a phenomenon that the version of FLASH (v2.5) that we used does not model. Note that the latest version of FLASH (currently v4.2) still does not model photoionization.

In this paper, we present column densities of Si IV (i.e., N(Si IV)) that result from hydrodynamic interactions between hot and cool gas in the TML and HVC geometries. These calculations were done for the same physical set-ups as in KS10 and KHS11 and, like the results presented in those papers, do not include the effect of photoionization. For this paper, we ran 13 additional FLASH runs (6 TML models like those in KS10 and 7 HVC models like those in KHS11) that trace the ionization states of silicon. Note that the hydrodynamic evolution of the new FLASH runs in which the ion fractions of silicon ions were traced is identical to those of the previous runs in which the ion fractions of the other three elements were traced[1]. The results for N(Si IV) predicted from the additional simulations are presented in a similar fashion as in KS10, KHS11, and HKS12. We compare our predictions of N(Si IV) with observations and predictions from other types of models. The new results for N(Si IV) complement the previous results for N(C IV), N(N V), and N(O VI) that were presented in KS10, KHS11, and HKS12.

In HKS12, we considered a composite model in which the halo has four possible sources of low-velocity high ions, including our modeled HVCs, supernova remnants, galactic fountains, and photoionization. With this composite model, we tried to account for the quantities of low-velocity C IV, N V, and O VI observed in the Milky Way's halo. This composite model was designed to explain the full quantity of observed low-velocity O VI and we found that this model could also account for most of the observed low-velocity C IV. In this paper, we apply a similar analysis of the possible sources of low-velocity Si IV by using the same composite model as in HKS12. Note that among the four high ions observed in the UV

[1] The hydrodynamics calculated by the simulations are independent of the element whose ions we chose to trace because our cooling algorithm determines the cooling rate resulting from the dozen most abundant elements and the assumption that their ions are in CIE (see KS10 for some discussion of CIE versus NEI cooling rates).

band, Si IV can be produced by the lowest energy photons[2]. Hence, a significant fraction of Si IV observed in the Milky Way's halo could be produced via photoionization as is the case with C IV. We find that an extra photoionization source which could increase only the number of low-velocity Si IV without affecting those of the other ions (especially C IV) would be required to explain the observed low-velocity Si IV. However, more detailed calculations that include more accurate modeling of the spectrum of ionizing photons will need to be carried out in order to explain the full amounts of low-velocity high ions in the halo. Note that photoionization can affect the amounts of high-velocity low ions such as C II, C III, Si II, and Si III in HVCs (Fox et al. 2005) because escaping photons from the Galactic disk could reach even distant HVCs such as the Magellanic Stream (Bland-Hawthorn & Maloney 1999).

In the next section, we will briefly summarize the TML and HVC models from which the Si IV column densities are predicted. The predicted Si IV column densities are presented in Sections 3 and 4, respectively. In Section 5, we compare our Si IV predictions with observations and with predictions made from other models. At the end of Section 5, we will discuss the effect of photoionization on the Si IV ions in the Galactic halo by including our new Si IV results in the composite scenario like that considered in HKS12. Section 6 summarizes our results.

2. Summary of NEI Simulations

The Si IV column densities that we present in this paper were calculated from new FLASH runs that modeled the same hydrodynamics as were modeled in KS10 and KHS11, with the only differences between the new and old FLASH runs being that silicon ionization levels were calculated in the new runs. In this section, we briefly summarize the basics of our previous two sets of simulations (TML from KS10 and HVC from KHS11). In the TML simulations, cool gas slid past hot gas. At the boundary, shear instigated instabilities that mixed the gas. An initial irregularity in the boundary between the two gases was used in order to seed the instabilities. In the reference model (TML Model A), the density and temperature of the cool and hot gas were chosen to match those of a cool cloud embedded in hot ambient gas in the Milky Way's halo ($T_{cool} = 10^3$ K, $n_{cool} = 0.1$ hydrogen atoms cm^{-3},

[2]The ionization potentials of Si III, C III, N IV, and O V, which are the energies to further ionize these ions to the next level of ionization, are 33, 48, 77, and 114 eV, respectively. Note that the ionizing radiation field from hot (O-type) stars in the Galactic disk can provide photons with energies up to 54 eV, the He II ionization edge, which are capable of photoionizing Si III to Si IV and C III to C IV, but are not capable of producing N V or O VI.

$T_{hot} = 10^6$ K, and $n_{hot} = 10^{-4}$ hydrogen atoms cm^{-3}; both cool and hot gas contain one helium atom per every 10 hydrogen atoms). The cool gas moved relative to the hot gas at a velocity of $v_x = 100$ km s^{-1}. The simulation ran for 80 Myr. A layer of mixed gas developed between the cool and hot gas layers and it broadened over time. In KS10, we reported that high ions such as C IV, N V, and O VI were abundant in the mixing layer; here, we report that Si IV is also abundant. We refer readers to KS10 for more details regarding the TML models.

In the HVC simulations, spherically shaped clouds moved relative to the surrounding hot ambient medium. To be precise, the hot ambient medium flowed through the grid, past the initially stationary cloud. (Having the hot medium move rather than having the cloud move allowed us to track the evolution for longer periods of time.) The cloud's material ablated due to shear instabilities and subsequently mixed with the hot ambient medium, forming mixed gas where the high ions became abundant. The reference model (HVC Model B) had the ISM with the same density and temperature as the TML reference model (TML Model A: $T_{ISM} = 10^6$ K, and $n_{ISM} = 10^{-4}$ hydrogen atoms cm^{-3}). The cloud's radius is approximately 150 pc and its density profile is shown in Figure 1 of KHS11. The cloud's temperature is determined from the cloud's density and the pressure balance with the ISM. Note that both cool and hot gas contain one helium atom per 10 hydrogen atoms and we assume that both hydrogen and helium are fully ionized regardless of the temperature during the simulation. The hot medium moved relative to the cloud at a velocity of 100 km s^{-1}. More details regarding the HVC models can be found in KHS11.

For this paper, we ran 13 additional FLASH runs tracing the ionization states of silicon (see Tables 1 and 2 for the model parameters of 6 TML models and 7 HVC models, respectively). The FLASH NEI modules used the default abundance of silicon which is from Landini & Monsignori Fossi (1990)[3] in these additional runs. However, the resulting column densities of Si IV (and other high ions such as C IV, N V and O VI) can be linearly re-scaled if different choices of abundances are desired, because the only effect of the chosen abundances on the results of our simulations is to change the total number of ions of a given element[4]. In this paper, we rescaled the calculated Si IV column densities using the interstellar silicon

[3] The silicon abundance in Landini & Monsignori Fossi (1990) is 2.63×10^{-5} (the ratio of silicon to hydrogen), which is different from that in Allen (1973, 3.31×10^{-5}).

[4]In principle, the abundances could also affect the hydrodynamics of the simulations through the cooling rates. However, note that in our current simulations (both TML and HVC simulations), the cooling rates were approximated with CIE cooling rates that were calculated from the abundances of Allen (1973). Here we assumed that variations in abundances would not affect the CIE cooling rates significantly.

abundance of Wilms et al. (2000)[5]. Note that KS10 and KHS11 assumed Allen (1973) cosmic abundances, whereas HKS12 (our most recent paper on this topic) assumed Wilms et al. (2000) interstellar abundances. The Wilms et al. (2000) abundances are in good agreement with recently measured and commonly used solar photospheric abundances (Asplund et al. 2009). For this reason, we also rescaled the column densities of other high ions (C IV, N V, and O VI) using the abundances of Wilms et al. (2000) for presentation in this paper.

3. N(Si IV) from the TML Simulations

Here we discuss turbulent mixing in general and the Si IV ions modeled in our six new TML simulations in particular. As the surface of a cool cloud slides across a reservoir of hot gas, shear instabilities (also known as Kelvin-Helmholtz instabilities) grow over time and as a result a mixing layer develops between the cold and hot regions. In this layer, material torn from the cool cloud mixes with hot gas and consequently rises in temperature and begins to ionize. Simultaneously, the portions of hot gas that mixed with ablated cloud material begin to cool (due to mixing and due to radiation), and recombine. Owing to the slower rates at which recombination and ionization occur, the ionization levels of the gas throughout the mixing layer get out of collisional ionization equilibrium and Si IV can be found throughout the mixed gas. Radiative cooling in the upper part of the mixing layer is particularly important, reducing its temperature to a few to ten times 10^3 K much quicker than the ions can recombine. The non-equilibrium effects are very strong here, such that the fraction of silicon ions that have lost 3 electrons is much larger than that of CIE gas at the same temperature. Figure 1 shows the fraction of Si ions that are in the Si IV level (the Si IV fraction) for a vertical slice through the domain at the end of the TML Model A simulation (80 Myr). At this time, the depth of the entire mixing layer is about 200 pc, of which the region from a height of $z = -50$ pc to $z = 0$ pc has cooled to a few to ten times 10^3 K and, as can be seen in the figure, still contains Si IV. Because shear instabilities still grow while the mixing layer develops, their features appear as the tendrils of the mixed gas in the region between $z \approx -100$ pc and $z \approx -200$ pc.

The mixing layer is also rich in the other high ions, as can be seen in Figure 1 of KS10. A closer comparison between our Figure 1 and Figure 1 of KS10, however, reveals that the evolution of Si IV resembles that of C IV more than those of the other ions. This is because the ionization potentials of Si III and C III are smaller and more similar to each

[5] The abundances of carbon, nitrogen, oxygen, and silicon (i.e., the number per one hydrogen atom) are 2.40×10^{-4}, 7.59×10^{-5}, 4.90×10^{-4}, and 1.86×10^{-5}, respectively, in Wilms et al. (2000).

other than those of N IV and O V. Similar ionization patterns between C IV and Si IV within the temperature range of 10^4 K to several times 10^5 K can be understood as a result of similar electronic configurations: $1s^2 2s^1$ for C IV (the valence electron feels a net charge of +4 because the carbon nucleus +6 charge is screened by the two inner electrons) and $1s^2 2s^2 2p^6 3s^1$ for Si IV (similarly, the valence electron feels a net charge of +4 because the silicon nucleus +14 charge is screened by 10 inner electrons).

The time evolution for N(Si IV) for TML Model A and for the other models in the suite of TML simulations is shown in Figure 2. The Si IV column densities increase rapidly with time early in the simulations, as the mixing zone thickens, but less rapidly or not at all after the midpoints of the simulations. The exception to this trend is TML Model F, which has a hotter ambient temperature than the other models and so its mixing zone requires more time to mature than in the other models. In general, the time evolution of N(Si IV) is similar to those of N(C IV), N(N V), and N(O VI), which are shown in Figures 2 and 6 of KS 10. However, the predicted column densities of Si IV are smaller than those of the other ions because the gas has a lower abundance of silicon than of carbon, nitrogen, or oxygen. The column densities of Si IV relative to those of C IV and O VI are shown in the ratio plots of Figure 3. As mentioned above, N(Si IV) and N(C IV) evolve similarly, thus the N(Si IV)/N(C IV) ratio remains roughly constant over time for most of the models. We calculate the mean, median, standard deviation, minimum, and maximum for N(Si IV)/N(C IV) and N(Si IV)/N(O VI) within a range of time and tabulate the results in Table 3.

4. N(Si IV) from HVC Simulations

In our HVC simulations, the initial spherical cloud loses its cool material due to shear instabilities that are developed across the boundary between the cloud and the ISM. As time goes by, the cold material ablated from the cloud mixes with the hot ambient gas and the mixed gas reaches intermediate temperatures due to both mixing and cooling. Figure 4 shows the time evolution of the Si IV ion fraction obtained from HVC Model B which is a reference model of our HVC simulations. As in the TML simulations, Si IV becomes abundant in the intermediate temperature gas that results from the mixing of hot ambient gas with cold gas ablated from the cloud (see Figure 2 of KHS11 for the time evolution of hydrogen number density, temperature, v_z, and ion fractions of other ions, C IV, N V, and O VI). Mixed gas forms a trail behind the cloud, with the mixed gas nearest to the cloud having approximately the same speed as the cloud and the mixed gas furthest from the cloud having slowed to approximately the rest frame of the environment. Thus, in our HVC

simulations, high ions including Si IV contained in the mixed gas are identified as either low- or high-velocity ions depending on the speed of the mixed gas relative to an observer in the rest frame of the environmental gas. Following the same convention as in KHS11 and HKS12, we distinguished the low- and high-velocity Si IV by using the same velocity criterion (80 km s^{-1} for HVC Models A, B, F, and G and 100 km s^{-1} for HVC Models C, D, and E)[6].

We present first the evolution of the amounts of low velocity and high velocity Si IV in the mixed gas in the domain for each of our HVC models. Figure 5 shows the mass of Si IV as a function of time and its evolution generally looks more similar to that of C IV (Figure 3 of HKS12) than to those of N V and O VI (Figures 4 and 5 of HKS12, respectively). In particular, in most models, the tallies of low-velocity C IV and Si IV that include escaped ions (i.e., ions that have escaped from the domain by flowing through the upper boundary of the domain) tend to be comparable to or smaller than those for the high-velocity C IV and Si IV, in contrast with the case of O VI, in which there tends to be more low velocity material than high velocity material at any given time. The resemblance in the mass evolution between C IV and Si IV, especially in comparison with O VI, can also be understood as being a result of carbon and silicon having similar ionization potentials.

Next, as in KHS11, we present the predicted column densities of high-velocity Si IV along vertical sightlines through the simulation domain. These column densities can be directly compared with observations. We show both the high-velocity N(Si IV) and the total, irrespective of velocity, N(Si IV) as functions of off-axis radius (Figures 6 and 7: note that we chose the same epochs for these plots as in Figures $7-9$ in KHS11). Figures 6 and 7 show that N(Si IV) is greatest along the sightline through the center of the cloud and that it generally decreases as the off-axis radius increases. A similar trend was found in the footprints of N(C IV), N(N V), and N(O VI) (see Figures 7, 8, and 9 of KHS11). However, a closer comparison again reveals a greater similarity between N(Si IV) and N(C IV), a similarity that is likely due to the similarity in the ionization potentials of silicon and carbon. For example, in the case of HVC Model B, the footprint and overall shape of the N(Si IV) plot (right panel in Figure 6) looks more similar to that of N(C IV) (top right panel in Figure 7 of KHS11) than to that of N(O VI) (bottom right panel in Figure 7 of KHS11).

[6]Our HVC simulations were conducted with the ambient gas flowing upwards ($+z$ direction) while the initial cloud was stationary. However, in both KHS11 and HKS12, we reported the velocities in the observer's reference frame, where the observer is assumed to be located below the domain and moves with the same velocity as the initial ambient gas. In the observer's frame, the initial cloud falls downwards ($-z$ direction). We refer to material that travels downwards (in the observer's reference frame) with a velocity that is significantly less than the designated HVC velocity as low velocity material and material that travels downwards at a faster velocity as high velocity material.

Not only are the column densities of the high-velocity Si IV predicted from our HVC models, but also the ratios of the column densities of high-velocity Si IV to the column densities of other high-velocity high ions are of great interest. For this reason, we present N(Si IV)/N(C IV) and N(Si IV)/N(O VI) for the high-velocity ions in Figure 8. Note that some material flows out of the domain, but most of this material has low velocity (relative to the observer). Thus, the column density ratios shown here, like those shown in Figure 11 of KHS11, were calculated only from the material within the computational domain. We also used the same column density cut-off (N_{cut}) for the calculation of the average column densities of Si IV in order to exclude the contribution from the backgroud gas to the average, and the column density ratios are taken after the average column densities of individual high-velocity high ions are calculated (see equations (2) and (3) in KHS11). As can be seen in Figure 8, the ratios of high-velocity Si IV to C IV and O VI do not vary significantly between models, regardless of the variations in model parameters in the set of HVC simulations (although HVC Model A shows an exceptional trend). This also occurred in the ratios of high-velocity C IV to O VI and N V to O VI (see Figure 12 in KHS11). Table 4 shows the mean, median, standard deviations, minimum, and maximum ratios obtained from Figure 8 within a range of time that excludes the early epochs of each simulation.

In HKS12, we calculated the quantities of low-velocity C IV, N V, and O VI that the Milky Way halo would acquire from infalling HVCs if real HVCs are like those in our simulations. These low-velocity high ions are in the gas that ablated from the clouds, mixed with the ambient medium, and slowed, sometimes to the velocity of the ambient medium. The average column density (per species) contribution of low-velocity ions due to infalling HVCs to the observed column densities in the Milky Way's halo was calculated by using equation (3) of HKS12,

$$\bar{N}(\mathrm{ion}) = \frac{\dot{\mathcal{M}}^{\mathrm{H}}_{\mathrm{HVC}}}{2\pi R^2_{\mathrm{MK}} M^{\mathrm{H\ I}}_{\mathrm{HVC},0} m_{\mathrm{ion}}} \int M_{\mathrm{ion}}(t) dt, \tag{1}$$

where $\bar{N}$(ion) is the average column density of a given ion along a vertical sightline, $\dot{\mathcal{M}}^{\mathrm{H}}_{\mathrm{HVC}}$ is the observation-constrained infall rate of high velocity clouds, R_{MK} is the radius of the Milky Way's disk, $M^{\mathrm{H\ I}}_{\mathrm{HVC},0}$ is the initial H I mass of each model cloud, and m_{ion} is the atomic mass of the given ion. We performed the calculation using $\dot{\mathcal{M}}^{\mathrm{H}}_{\mathrm{HVC}} = 0.5 M_{\odot}$ yr^{-1} for consistency with HKS12 and $\dot{\mathcal{M}}^{\mathrm{H}}_{\mathrm{HVC}} = 1.0 M_{\odot}$ yr^{-1} in light of more recent infall rate estimates (see Section 5.2). We took R_{MK} to be 25 kpc as in HKS12. Following the same approach that HKS12 used for C IV, N V, and O VI (see Section 4 of HKS12), we first integrated $M_{\mathrm{Si\ IV}}(t)$ (shown in Figure 5) with respect to time over the whole length of each simulation. Then, we used the resulting integral in Equation (1) which estimates the average column density of low-velocity Si IV in the Milky Way's halo.

The use of hydrocode simulation results in this calculation is complicated by the facts that some of the mixed gas flows out of the domain late in the simulated timespan and that the simulation timespan ends before the high ions have completely disappeared. We have attempted to compensate for these effects when preparing our tabulations of the average column densities (Table 5).

We present four families of estimates. The first two estimates are 'Domain only' (column [2] in Table 5) and 'Domain + Escaped' (column [3] in Table 5) under the category 'Average N(Si IV) during the simulations'. As in HKS12, the first estimates, i.e., the column densities listed under the category 'Average N(Si IV) during the simulations' and labeled 'Domain only' (column [2] in Table 5) use the low-velocity Si IV only present in the simulational domain (i.e., the time integration is calculated from the blue dotted lines in Figure 5), while the second estimates, i.e., the column densities labeled 'Domain + Escaped' (column [3] in Table 5) use this 'Domain only' Si IV plus low-velocity Si IV that has escaped from the domain during the simulation time (i.e., the time integration is calculated from the blue solid lines in Figure 5 during the simulation time). Because 'Domain + Escaped' ion column densities take into account the 'Escaped' ions, the 'Domain only' and 'Domain+Escaped' ion column densities generally correspond to lower and upper limits, respectively, of the contribution from the clouds during the simulation time.

However, the first two estimates, i.e., the column densities listed under the category 'Average N(Si IV) during the simulations', are still smaller than the true column densities because the simulations ended before all the material of the initial cloud (assumed to be neutral, initially) disappeared. Therefore, in addition to these quantities, we also present the last two columns of estimates of the four families, i.e., the average Si IV column densities calculated with the cloud's lifetime taking into account: 'Domain only' (column [5] in Table 5) and 'Domain + Escaped' (column [6] in Table 5) under the category 'Average N(Si IV) during the cloud's lifetime'. In order to account for the clouds' contributions throughout their entire lives, we followed HKS12 and assumed that the amounts of low-velocity high ions produced by the cloud are proportional to the mass of the cloud that is "removed" from the initial cloud by either ablation or ionization. In this case, the time integral $\int M_{\rm Si\ IV}(t)dt$ (integrated over the entire life of the cloud) in Equation (1) can be replaced by $\int_0^{T_{\rm sim}} M_{\rm Si\ IV}dt/\beta_{\rm HVC}$, where $\beta_{\rm HVC} = M^{\rm H\ I}_{\rm HVC,lost}/M^{\rm H\ I}_{\rm HVC,0}$ is the fraction of the initial cloud mass that is "lost" due to either ablation or ionization by the end of the simulation (HKS12). Thus, the estimated column densities (columns [2] and [3] in Table 5) divided by $\beta_{\rm HVC}$ (tabulated in both Table 2 of HKS12 and Table 5 of this paper) yield better estimates. Columns [5] and [6] in Table 5 are obtained by dividing columns [2] and [3] by $\beta_{\rm HVC}$, respectively. These values for Si IV can be compared with the results for C IV, N V, and O VI in Table 2 of HKS12.

5. Comparison with Observations and Other Models

In this section, we compare our predicted Si IV column densities with observations and predictions from other models. Gas in and near the Galaxy is generally classified as high velocity ($|v_{LSR}| \gtrsim 90$ km s^{-1}) or low velocity ($|v_{LSR}| \lesssim 30$ km s^{-1}). (Although velocities between 30 and 90 km s^{-1} are also commonly termed intermediate velocities, for convenience, we include this range in our low velocity range.) Here, we make the same distinction, comparing our results with other models and observations of high velocity ions in Section 5.1 and comparing our results with other models and observations of low velocity ions in Section 5.2. While making our predictions, we consider only the vertical component of the velocity along vertical sight lines through the simulational domains. Only the HVC simulations have Si IV with large vertical velocities. Both the HVC and the TML simulations have Si IV with low vertical velocities, because material ablated from the cloud is able to decelerate in the HVC simulation and because the cloud's motion is in the horizontal direction in the TML simulation.

5.1. High-Velocity Si IV

For the observed column densities of high-velocity Si IV, we use the results of Shull et al. (2009), where column densities of high- and intermediate-velocity Si IV (along with Si II and Si III) toward 37 AGNs at high Galactic latitudes were reported. Note that the study of Shull et al. (2009) is the largest collection of high-velocity Si IV measurements to date. For comparison with the predictions of our HVC models, we consider only the detected high-velocity components in Table 2 of Shull et al. (2009). There are 37 such detections (note that on some sightlines there are no detections, and on others more than one). The average, median, standard deviation, minimum, and maximum of logarithmic column densities of high-velocity Si IV, log[N(Si IV)], are 12.81, 12.77, 0.34, 11.98, and 13.51, respectively, for the sample composed of 37 detections (i.e., excluding non-detections and counting mutiple detections separately along the same sightline).

Comparing such values with our simulational results is not so simple. For a collection of vertical sightlines through the simulational domain, in general, the predicted high-velocity N(Si IV) peaks near the central sightline, remains sizeable for sightlines within two times the initial cloud radius, and decreases along the sightlines at larger off-axis radii from the central sightline (Figures 6 and 7). Although the predicted column densities of high-velocity Si IV vary along wide ranges of sightlines at different epochs, some of them are consistent with the observations. For example, in cases of HVC Models B, C, D, and E (whose initial cloud radii are ~ 150 pc), the predicted high-velocity N(Si IV) reaches slightly above 10^{13} cm^{-2}

along the central sightline (i.e., $r \sim 0$ pc), especially at later times. Along the sightlines at larger off-axis radii in these models (i.e., $r \sim 150 - 200$ pc) at $t = 120$ Myr, the predicted high-velocity N(Si IV) is still above 10^{12} cm^{-2}, which is also consistent with the minimum observed value. Similar overlap between predictions for sightlines that pass vertically through a single HVCs shroud and observations can be found for HVC Model A (whose initial cloud radius is ~ 20 pc), HVC Model G (which has an order of magnitude lower density than HVC Models B to E), and HVC Model F (which has the largest radius, ~ 300 pc), for a range of sightlines at some selected times.

However, note that the central sightline is only a small fraction of the cross section of the modeled HVC structure and that the column densities along sightlines at larger off-axis radii from the central sightline are often outside the observed range. Thus, if we were to take into account the effect of averaging the predicted column densities over all of the sightlines that intersect the cloud (instead of comparing the predicted column density along a specific sightline at a given time with the observations as above), reality would often show higher column densities than our HVC models. This is shown in Figure 9, where we compare the observed distribution of Si IV column densities with the average Si IV column density of high vertical velocity gas in our HVC models as a function of time. To distinguish sightlines that contain Si IV from those that do not, we excluded sightlines whose Si IV column densities fall below our cut-off (N_{cut}), which is 10^{11} cm^{-2} for HVC Models B through F and 10^{10} cm^{-2} for HVC Models A and G.

Even regions in our modeled HVC structures having only marginal amounts of Si IV could contribute to the observed Si IV column densities if multiple HVC structures exist along the observed lines of sight. Such HVCs need not be on the size scale of the named complexes, but could be cloudlets within a complex, and the structures could include ablated material behind the infalling clouds. The ablated material may be ionized and so not readily counted in H I surveys. Although it is possible to postulate such a multiple-cloud model, the number of HVC structures along any given line of sight could be difficult to constrain. For this reason, it is more practical to compare the ratios of the Si IV, C IV, and O VI column densities to those garnered from the observations and those extracted from other models.

Figure 10 compares the observed N(Si IV)/N(O VI) and N(C IV)/N(O VI) ratios with those from our models and from other models, a shock heated gas model and two radiatively cooling gas models. First of all, our HVC models predict the observations very well. Some predictions from other models, such as a shock heating model (Dopita & Sutherland 1996, two data points in the upper-right region correspond to their models having the highest two shock speeds, 400 and 500 km/s, and largest magnetic field) are close to the observations, too. Note that although the radiative cooling model including the isochoric non-equilibrium

ionization (Gnat & Sternberg 2007, dashed orange line) matches the observed ratios of high-velocity ions when the temperature reaches an approximate range of $(1.4-2.2)\times10^4$ K (note that the temperature decreases along all three orange lines from lower-left to upper right), these predictions are more relevant to the ratios of low-velocity ions which we will discuss in the following section.

5.2. Low-Velocity Si IV

Both our TML and HVC models predict low-velocity Si IV that can be compared with observed Si IV in the halo of the Milky Way. In our TML simulations, in order to sample the mixed zone most effectively, our simulated lines of sight pass perpendicularly through the mixed zone and are perpendicular to the direction of motion of the cool cloud. As a result, all of the Si IV in the domain appears to have low velocities. In contrast, the low-velocity Si IV in our HVC simulations, resides in mixed gas that has slowed to low-velocities (< 80 km s^{-1} for HVC Models A, B, F, and G and < 100 km s^{-1} for HVC Models C, D, and E) and is observed along sightlines that are parallel to the direction of motion of the HVC. We first compare the low-velocity Si IV observed on Milky Way halo lines of sight with those predicted from our TML simulations and then we compare with the column density of decelerated Si IV expected to result from a population of HVCs. The ratios of Si IV to O VI, Si IV to C IV, and C IV to O VI column densities form the basis of another important test, which we then perform. Furthermore, the high ions in the halo may be due to multiple causes and therefore, later in this section, we add our new Si IV results to the composite scenario for low-velocity high ions in the halo that was presented in HKS12 and compare with observations.

To determine the average column density of low-velocity Si IV observed in the Milky Way, we use the results of Wakker et al. (2012), where column densities of low-velocity Si IV (along with O VI, N V, C IV, and Fe III) toward 58 extragalactic objects were reported. Note that the study of Wakker et al. (2012) includes the largest number of observed sightlines for the low-velocity high ions to date. Along a given observed line of sight, Wakker et al. (2012) presented both the component column densities within certain ranges of velocities and the integrated column densities which sum up the component column densities within a wider range of velocities. Because the predicted column densities from our model calculations are also integrated over a wide range of velocities, we compare our predictions with the integrated column densities from Wakker et al. (2012). The average of the integrated Si IV column densities from Wakker et al. (2012, not latitude corrected) is $\sim 3.7\times10^{13}$ cm^{-2}, while the typical Si IV column density predicted from sightlines oriented perpendicular to the single

hot-cool interface in each of our TML Models A, B, D, E, and F is about 10^{12} cm^{-2}. In TML Model C (which examined turbulent mixing on smaller scales over shorter time periods and has an order of magnitude smaller domain than the other TML models), the average Si IV colum density calculated over the time interval of $[6, 8]$ Myr is $\sim\ 1.3 \times 10^{11}$ cm^{-2}. (Note that at a given time, the spatially averaged column density is calculated first and then the temporal average of spatially averaged column densities over the given time intervals is calculated. The average column density for TML Model C is calculated in this way.) If all of the observed low-velocity Si IV in the halo is due to TMLs, then 37 layers like those in TML Models A, B, D, E, and F or 280 layers like those in TML Model C, are required to be along the average line of sight[7]. Note that, because the low-velocity Si IV scale height is a few kiloparsecs (Savage & Wakker 2009), and the mixing layers in our TML models are typically ~ 100 pc thick (~ 10 pc for TML Model C), it may be difficult to fit the required number of mixing layers along the line of sight.

We now consider the column densities of low-velocity Si IV in decelerated gas ablated from HVCs. Here, rather than examining the contribution of a single HVC, we consider the effect of an ensemble of HVCs that are like our model HVCs (i.e., the model calculated in Section 4 and tabulated in Table 5). The predicted column densities are compared with the average observed column density in Figure 11. For the average observed column density, we again use the Si IV results from Wakker et al. (2012). Figure 11 shows that the predicted low-velocity N(Si IV) severely underpredicts the observed N(Si IV). Even the largest prediction ($\sim 5.4 \times 10^{12}$ cm^{-2} estimated with an HVC infall rate $\dot{\mathcal{M}}^{\rm H}_{\rm HVC} = 1.0 M_\odot$ yr^{-1}) which is from a population of clouds like those in HVC Model F and includes both the ions that have escaped from the domain and the effect of the lifetime evolution of the cloud, is smaller than the average observed value by a factor of ~ 5. A similar comparison for the C IV, N V, and O VI ions was done in HKS12 (with an HVC infall rate $\dot{\mathcal{M}}^{\rm H}_{\rm HVC} = 0.5 M_\odot$ yr^{-1}), where we concluded that the model was better at explaining the observed O VI than at explaining the observed N V or C IV (this conclusion does not change even with a factor 2 larger infall rate $\dot{\mathcal{M}}^{\rm H}_{\rm HVC} = 1.0 M_\odot$ yr^{-1}).

As mentioned earlier, comparing the ratios of column densities of multiple high ions, such as Si IV to O VI, between observations and predictions is a better method for constraining the models. The comparison for the low-velocity high ions is shown in Figure 12, including

[7] The average integrated column densities of C IV and O VI obtained from Wakker et al. (2012) are $\sim 1.5 \times 10^{14}$ cm^{-2} and $\sim 2.0 \times 10^{14}$ cm^{-2}, respectively, while the predicted column densities of these two ions from our TML models (except TML Model C) are $\sim 7.3 \times 10^{12}$ cm^{-2} and $\sim 4.4 \times 10^{12}$ cm^{-2}, respectively. Thus, approximately 20 and 45 layers are required to explain the observed column densities of the C IV and O VI ions, respectively.

the predictions from our TML models and the decelerated gas in our HVC simulations. First of all, it is interesting to recognize that the observed ratios are clustered more tightly than the model predictions. In this plot, the predictions from our TML models (purple triangles) and the galactic fountain model (cyan squares) are in good agreement with the observations. However, careful comparison between the predictions of our TML models and the observations shows that the predicted N(C IV)/N(O VI) ratio is slightly larger than the central value of the observed ratios by about 0.3 dex, while the predicted N(Si IV)/N(O VI) ratio is similar to the central value of the observed ratios. Note that this is consistent with the disparity in the aforementioned estimates of the numbers of layers that are required to explain the observed column densities of these three ions, i.e., 20, 37, and 45 layers for C IV, Si IV, and O VI, respectively. Some predictions from supernova remnant models (Shelton 2006, green triangles) at late phases of the evolution overlap or are close to the observations, but there is a tendency for this model to slightly underpredict the N(Si IV)/N(O VI) ratio. The predictions from the isochoric radiative cooling model that includes non-equilibrium ionization (Gnat & Sternberg 2007, dashed orange line) match the observations well in the $(1.4 - 2.2) \times 10^4$ K temperature range (note again that the temperature decreases along all three orange lines from lower-left to upper right). All the other models including our HVC models (blue squares) either significantly underpredict the N(Si IV)/N(O VI) ratio or, as in the cases of the CIE radiative cooling (Gnat & Sternberg 2007; Sutherland & Dopita 1993, at $T \gtrsim 1.7 \times 10^5$ K), overpredict the N(C IV)/N(O VI) ratio.

Recently, Wakker et al. (2012, their Section 5, in particular, their Figure 11) made a detailed comparison for the ratios of column densities of low-velocity high ions between various model predictions and observation data sets that they collected and analyzed. What they found from their comparison is quite similar to our results discussed above[8]: our TML models, the galactic fountain, and the non-equilibrium radiative cooling model (with $T \sim 1 - 2 \times 10^4$ K) are favored. Note that in all three of these models ionization of interesting atoms is calculated in the non-equilibrium fashion (this is also true for the case of the ratios of high-velocity high ions). Thus, including the non-equilibrium ionization calculation is essential in the modeling of whatever physical processes are relevant to the production of high ions.

As shown in Figure 12, our models of the decelerated gas following HVCs underpredict the column densities of low-velocity C IV and Si IV with respect to those of low-velocity O VI. Note that both C III and Si III ions are more susceptible to photoionization than

[8] Wakker et al. (2012) re-scaled all the model predictions according to the abundances of Asplund et al. (2009) which have more carbon and silicon by 0.05 and 0.24 dex, respectively, than those of Wilms et al. (2000). The abundances of oxygen are almost identical in both references.

the O V ions, but our HVC simulations have the limitation that they did not include the effect of the photoionization. Photoionization is astrophysically important and suspected of boosting the C IV and Si IV contents of the gas over those predicted in our simulations. For this reason, we suggested a composite model in HKS12 which combines together four model sources for low-velocity high ions, in order to attempt to explain the full amounts of the observed low-velocity high ions. Note that in HKS12 we did not expect that our HVC models alone could explain the full amounts of observed low-velocity high ions. (We would like to remind readers that the primary purpose of our estimating the amounts of low-velocity high-ions from our HVC models in HKS12 is to quantitatively measure the contribution from this model to the total amounts.) The composite model was composed of contributions from the following four sources of high ions: slowed ablated gas from a population of HVCs like our HVC Model B, a population of extraplanar supernova remnants (Shelton 2006), galactic fountains (Shapiro & Benjamin 1993), and photoionization by an external radiation field (Ito & Ikeuchi 1988). Choosing these four sources may be justified by a dynamic picture of the Galactic halo, where these four sources work as independent sources of high ions while disturbing the halo in different ways.

Table 6 presents the updated results of our composite model, with the new Si IV calculations included (cf. Table 3 of HKS12). First of all, note that the composite model is designed to reproduce the observed O VI column density. In order to reflect the most updated observational data, we used the results from Wakker et al. (2012). We calculated the average $N \sin |b|$ for all four ions from their Table 2, considering only the integrated column densities along the detected sightlines. Note also that all of the model predictions in Table 6 are re-scaled using the elemental abundances of Wilms et al. (2000) (in Table 3 of HKS12, the re-scaling has not been done to the model predictions). However, these adjustments do not alter the conclusions of HKS12: the composite model reproduces most of the observed C IV column density, but underpredicts the observed N V column density. The model also underpredicts the observed Si IV column density; the discrepancy between the predicted and observed values is more severe than for N V. (The contribution to Si IV from the SNR model was not included in Table 6 because it was not available. However, its contribution is not expected to be large enough to change the overall conclusion.) The severe shortage of Si IV in the composite model occurs because the models that exclude photoionization tend to underpredict Si IV to an extent that is not fully compensated for by the chosen photoionization model. However, the referenced photoionization model (i.e., Ito & Ikeuchi 1988), was not well constrained, allowing the possibility that more Si IV has resulted from photoionization than thought.

The amounts of high ions produced via photoionization depend on the spectrum of ionizing photons. For example, Ito & Ikeuchi (1988) used a simple power-law spectrum such

as $I(\nu) = I_0(\nu/\nu_T)^{-1}$, where I_0 is the intensity at the Lyman limit of hydrogen, ν_T. They also assumed that this spectrum does not change spatially in the Galactic halo. However, it may be possible to increase the amount of Si IV, only, without affecting those of the other high ions (especially, the amount of C IV which is also susceptible to photoionization) by changing the spectrum of ionizing photons. Note that the ionization potential of Si III (33 eV) is slightly lower than that of C III (48 eV). Thus, if the spectrum of ionizing photons were dominated by photons with energy between these two ionization potentials, only the amount of Si IV would increase. Testing whether such a spectrum is physically realistic, and whether such a spectrum could indeed bring the Si IV column density in line with the observations, is beyond the scope of the current paper, but could be addressed in a future study.

Finally, it is worth mentioning again the effect of uncertain infall rates of HVCs on the predictions of low-velocity high ions that were made from our HVC models. HKS12 quoted several observationally based estimates. In addition to those, we would like to add $\sim 0.1\ M_\odot\ \mathrm{yr}^{-1}$ from H I HVCs (Putman et al. 2012), $0.1 - 1.4\ M_\odot\ \mathrm{yr}^{-1}$ from ionized HVCs (Lehner & Howk 2011), and $\sim 1\ M_\odot\ \mathrm{yr}^{-1}$ from Si III HVCs (Shull et al. 2009). Furthermore, a recent estimate of the ionized mass of the Magellanic System implies that the mass infall rate of this system alone is as large as $\sim 3.7 - 6.7\ M_\odot\ \mathrm{yr}^{-1}$ (Fox et al. 2014). In the current paper, we use both $\dot{\mathcal{M}}^{\mathrm{H}}_{\mathrm{HVC}} = 0.5 M_\odot\ \mathrm{yr}^{-1}$, for consistency with our earlier work in HKS12 and $\dot{\mathcal{M}}^{\mathrm{H}}_{\mathrm{HVC}} = 1.0 M_\odot\ \mathrm{yr}^{-1}$, in light of the more recent estimates.

The effect of increasing the mass infall rate is to increase the column densities of infalling high ions by a factor of 2, such that the values in Figure 11 and Table 5 are doubled, while the ion ratios for infalling material are not affected. The effect on the composite model is slightly complicated because the contribution from galactic fountains is calculated based on the assumption that the observationally determined average O VI column density would equal the sum of the contributions from HVCs, extraplanar SNRs, and galactic fountains. Therefore, the contribution from galactic fountains decreases when the assumed HVC infall rate increases. The contributions from extraplanar SNRs and photoionization by an external radiation field are not affected by the change in assumed HVC infall rate and photionization does not contribute to the N V or O VI column densities. In Table 6, we present the various components of our composite model for both the originally assumed HVC infall rate and the revised, higher rate (these new predictions are in parentheses underneath the original predictions). By affecting the calculated fountain contribution, the increased infall rate decreases the total Si IV and C IV column densities predicted by the composite model, while increasing the total predicted N V column density. Thus, the revised composite model does not account for the observed C IV as well as the original.

6. Summary

We have presented the column densities of Si IV predicted from two sets of hydrodynamic simulations: TML and HVC simulations. In the TML simulations which are carried out in 2D Cartesian coordinates, the column densities are calculated along the lines of sight that are perpendicular to the initial interface between the cool cloud and the hot ambient gas. The HVC simulations, carried out in 2D cylindrical coordinates, model cool spherical clouds falling through a hot ambient medium. In the HVC simulations, the column densities are calculated along the vertical lines of sight parallel to the initial velocity vector of the cloud assuming that the observers are located below the clouds. As in KS10, KHS11, and HKS12 which presented the C IV, N V, and O VI predictions, the quantities of Si IV ions in our simulations were calculated in a non-equilibrium fashion, i.e., the ionization states were updated at each hydrodynamic time step. Our calculations did not include photoionization. As a result, the predicted quantities of Si IV can be seen as lower bounds on the quantities that would exist in an environment that is affected by both the hydrodynamics of mixing and photoionization.

In both the TML and the HVC simulations, Si IV became abundant in the mixed gas that forms via mixing of cool cloud gas with the hot ambient gas, just as C IV, N V, and O VI did. The general features of the predicted Si IV ions in both the TML and the HVC simulations are more similar to those of C IV than to those of N V and O VI. There are three examples of this: (1) the time evolution of the high ion column densities in the TML models (Section 3), (2) the growth in quantities of high ions as a function of time in the HVC models (Section 4), and (3) the ion column densities as a function of off-axis radius in the HVC models (Section 4). This is likely because neutral silicon ($1s^2 2s^2 2p^6 3s^2 3p^2$) has a similar electron configuration to neutral carbon ($1s^2 2s^2 2p^2$) thus the ionization process to ionize Si III to Si IV is more similar to that to ionize C III to C IV than to those for N IV to N V or O V to O VI.

We compared the Si IV column densities extracted from the simulations with observations. The observational data can be categorized into high velocity ($|v_{LSR}| \gtrsim 90$ km s^{-1}) or low velocity ($|v_{LSR}| \lesssim 30$ km s^{-1}) regimes but, for convenience, we combine the low and intermediate velocity ranges to a single range encompassing $|v_{LSR}| \lesssim 90$ km s^{-1} and refer to it as low velocity. We compare the observed high velocity column densities with the predicted column densities from high velocity material in our HVC simulations and we compare the observed low velocity column densities with those of the decelerated gas in our HVC models and with the column densities on sightlines that are perpendicular to the direction of motion in our TML simulations. We found that the predictions for the high-velocity Si IV from our HVC models are in good agreement with the observations. Although the

column densities of high-velocity Si IV calculated along the chosen lines of sight from our HVC models vary widely from model to model (from $< 10^{11}$ cm^{-2} to a few times 10^{13} cm^{-2}), there is overlap between the predicted high-velocity column densities and those observed (up to 3.2×10^{13} cm^{-2}, Shull et al. 2009). However, when our predictions are time and space averaged and normalized by the observed population of HVCs, the resulting quantity of high velocity Si IV is less than that observed (Section 5.1 and Figure 9). We also compared the ratios of column densities of high-velocity high ions, N(Si IV)/N(O VI) against N(C IV)/N(O VI) because comparing the ratios of column densities of different ions provides a useful diagnostic to constrain models. We found that our HVC models also do a better job of predicting these ratios than a general shock heating model (Figure 10).

Most of our TML models predict low-velocity N(Si IV)$\sim 10^{12}$ cm^{-2} (the exception is TML Model C, which predicts $\sim 10^{11}$ cm^{-12}) so a few tens of layers would be required if TMLs alone were to explain the typical column density of low-velocity Si IV observed in the Milky Way's halo. Given the scale height of Si IV, it may be difficult to fit the required number of layers along the line of sight. We also calculated the average column densities of low-velocity Si IV predicted from each of our HVC models. We found that our individual HVC model clouds produce less decelerated Si IV than is actually observed on individual sightlines through the halo.

We also compared the ratios between low-velocity N(Si IV), N(C IV), and N(O VI) that are predicted from various models including our TML and HVC models and the ratios garnered from observations. We found that our TML models predict well the ratios of low-velocity ions. However, our HVC models underpredict the ratios of both N(Si IV)/N(O VI) and N(C IV)/N(O VI) for the low-velocity ions because the relative amounts of Si IV and C IV decrease more quickly than those of O VI in the decelerated mixed material. Some other models such as the galactic fountain, isochoric radiatively cooling, non-equilibrium ionization gas in the few times 10^4 K temperature regime, and the late stages of supernova remnant evolution are also in agreement with the low-velocity high ions. As other researchers did (e.g., Wakker et al. 2012), we pointed out the fact that all these "good" models include the effect of non-equilibrium ionization (which is also true for the high-velocity high ions), so it is essential to include the non-equilibrium ionization process in modeling the production of high ions.

We constructed a model for the low-velocity Si IV like the model for the low-velocity C IV, N V, and O VI in HKS12, in which an ensemble of HVCs passes through the halo, shedding gas that mixes with halo gas, and the mixed, high-ion-rich gas decelerates to the speed of the halo. This model explains a much smaller fraction of the observed Si IV than of the observed O VI (e.g., 2% versus 35% for HVC Model B). We then considered the

same composite model as in HKS12, in which HVCs are one of four sources of low-velocity high ions in the halo (the other sources being extraplanar SNRs, galactic fountains, and photoionization by an external radiation field). By design, the composite model accounts for all of the observed low-velocity O VI. HKS12 showed that it can also account for most of the observed low-velocity C IV. However, this model accounts for less than half of the observed low-velocity Si IV.

This shortfall in Si IV might be avoided if the ionizing radiation were to have a softer spectrum than that used in the photoionized model component. In that case, photoionization would preferentially produce Si IV.

We are grateful to the anonymous referee for his/her helpful comments that improved the original manuscript. The FLASH code used in this work was in part developed by the DOE-supported ASC/Alliance Center for Astrophysical Thermonuclear Flashes at the University of Chicago. The simulations were performed at the Research Computing Center (RCC) of the University of Georgia. This work was supported through grant NNX09AD13G through the NASA ATPF program. KK was also supported by Basic Science Research Program through the National Research Foundation of Korea (NRF) funded by the Ministry of Science, ICT, and Future Planning (NRF-2014R1A1A1006050).

REFERENCES

Allen, C. W. 1973, Astrophysical quantities (London: University of London, Athlone Press)

Asplund, M., Grevesse, N., Sauval, A. J., & Scott, P. 2009, ARA&A, 47, 481

Bland-Hawthorn, J., & Maloney, P. R. 1999, ApJ, 510, L33

Boehringer, H., & Hartquist, T. W. 1987, MNRAS, 228, 915

Borkowski, K. J., Balbus, S. A., & Fristrom, C. C. 1990, ApJ, 355, 501

Bowen, D. V., Jenkins, E. B., Tripp, T. M., et al. 2008, ApJS, 176, 59

Collins, J. A., Shull, J. M., & Giroux, M. L. 2004, ApJ, 605, 216

—. 2005, ApJ, 623, 196

—. 2007, ApJ, 657, 271

Cowie, L. L., Taylor, W., & York, D. G. 1981, ApJ, 248, 528

Dopita, M. A., & Sutherland, R. S. 1996, ApJS, 102, 161

Edgar, R. J., & Chevalier, R. A. 1986, ApJ, 310, L27

Fox, A. J., Savage, B. D., Wakker, B. P., et al. 2004, ApJ, 602, 738

Fox, A. J., Wakker, B. P., Barger, K. A., et al. 2014, ApJ, 787, 147

Fox, A. J., Wakker, B. P., Savage, B. D., et al. 2005, ApJ, 630, 332

Fox, A. J., Wakker, B. P., Smoker, J. V., et al. 2010, ApJ, 718, 1046

Fryxell, B., Olson, K., Ricker, P., et al. 2000, ApJS, 131, 273

Ganguly, R., Sembach, K. R., Tripp, T. M., & Savage, B. D. 2005, ApJS, 157, 251

Ganguly, R., Sembach, K. R., Tripp, T. M., Savage, B. D., & Wakker, B. P. 2006, ApJ, 645, 868

Gnat, O., & Sternberg, A. 2007, ApJS, 168, 213

Grevesse, N., & Anders, E. 1989, in American Institute of Physics Conference Series, Vol. 183, Cosmic Abundances of Matter, ed. C. J. Waddington, 1–8

Henley, D. B., Kwak, K., & Shelton, R. L. 2012, ApJ, 753, 58 (HKS12)

Ito, M., & Ikeuchi, S. 1988, PASJ, 40, 403

Jenkins, E. B. 1978a, ApJ, 219, 845

—. 1978b, ApJ, 220, 107

Kwak, K., Henley, D. B., & Shelton, R. L. 2011, ApJ, 739, 30 (KHS11)

Kwak, K., & Shelton, R. L. 2010, ApJ, 719, 523 (KS10)

Landini, M., & Monsignori Fossi, B. C. 1990, A&AS, 82, 229

Lehner, N., & Howk, J. C. 2011, Science, 334, 955

Lehner, N., Zech, W. F., Howk, J. C., & Savage, B. D. 2011, ApJ, 727, 46

Oegerle, W. R., Jenkins, E. B., Shelton, R. L., Bowen, D. V., & Chayer, P. 2005, ApJ, 622, 377

Putman, M. E., Peek, J. E. G., & Joung, M. R. 2012, ARA&A, 50, 491

Savage, B. D., & Massa, D. 1987, ApJ, 314, 380

Savage, B. D., Meade, M. R., & Sembach, K. R. 2001a, ApJS, 136, 631

Savage, B. D., & Sembach, K. R. 1994, ApJ, 434, 145

Savage, B. D., Sembach, K. R., & Howk, J. C. 2001b, ApJ, 547, 907

Savage, B. D., Sembach, K. R., & Lu, L. 1997, AJ, 113, 2158

Savage, B. D., Sembach, K. R., Wakker, B. P., et al. 2003, ApJS, 146, 125

Savage, B. D., & Wakker, B. P. 2009, ApJ, 702, 1472

Sembach, K. R., & Savage, B. D. 1992, ApJS, 83, 147

Sembach, K. R., Savage, B. D., & Tripp, T. M. 1997, ApJ, 480, 216

Sembach, K. R., Wakker, B. P., Savage, B. D., et al. 2003, ApJS, 146, 165

Shapiro, P. R., & Benjamin, R. A. 1993, in Star Formation, Galaxies and the Interstellar Medium, ed. J. Franco, F. Ferrini, & G. Tenorio-Tagle, 275–280

Shelton, R. L. 2006, ApJ, 638, 206

Shull, J. M., Jones, J. R., Danforth, C. W., & Collins, J. A. 2009, ApJ, 699, 754

Shull, J. M., Stevans, M., Danforth, C., et al. 2011, ApJ, 739, 105

Slavin, J. D., & Cox, D. P. 1992, ApJ, 392, 131

Slavin, J. D., Shull, J. M., & Begelman, M. C. 1993, ApJ, 407, 83

Sterling, N. C., Savage, B. D., Richter, P., Fabian, D., & Sembach, K. R. 2002, ApJ, 567, 354

Sutherland, R. S., & Dopita, M. A. 1993, ApJS, 88, 253

Wakker, B. P., Savage, B. D., Fox, A. J., Benjamin, R. A., & Shapiro, P. R. 2012, ApJ, 749, 157

Wilms, J., Allen, A., & McCray, R. 2000, ApJ, 542, 914

Zsargó, J., Sembach, K. R., Howk, J. C., & Savage, B. D. 2003, ApJ, 586, 1019

This preprint was prepared with the AAS LaTeX macros v5.2.

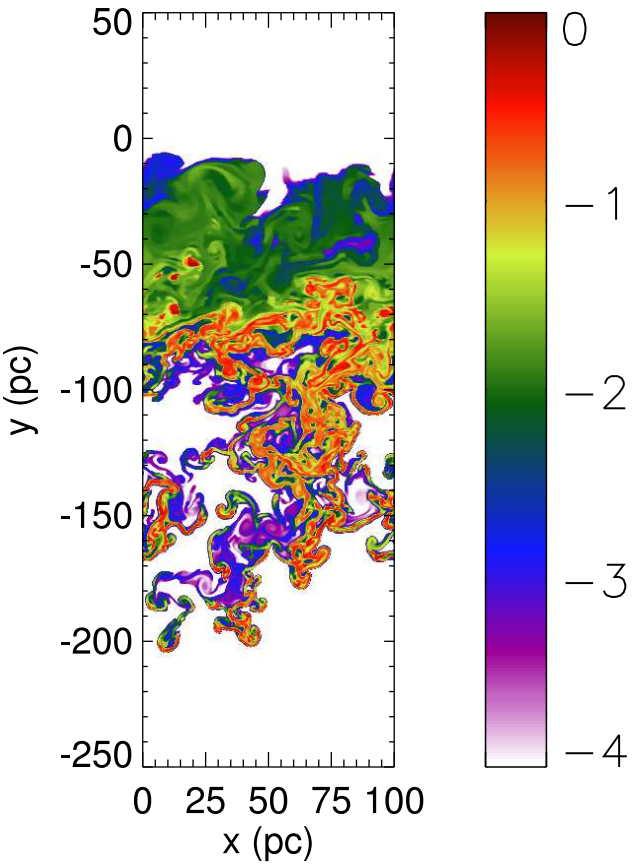

Fig. 1.— The Si IV ion fraction (on a logarithmic scale) from TML Model A at t=80 Myr.

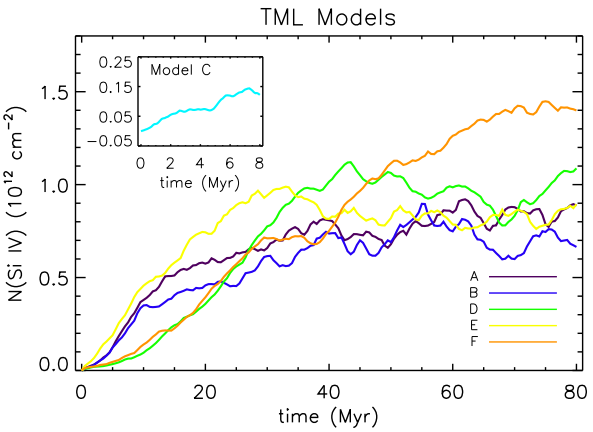

Fig. 2.— Time evolution of the Si IV column densities for the TML models. The column densities at each epoch were obtained after averaging over many, evenly spaced, vertical sightlines through the domain (256 sightlines for Models A, B, D, E, and F and 512 sightlines for Model B), i.e., sightlines parallel to the y-axis at different x locations in Figure 1. The inset is for Model C, which ran to t=8 Myr.

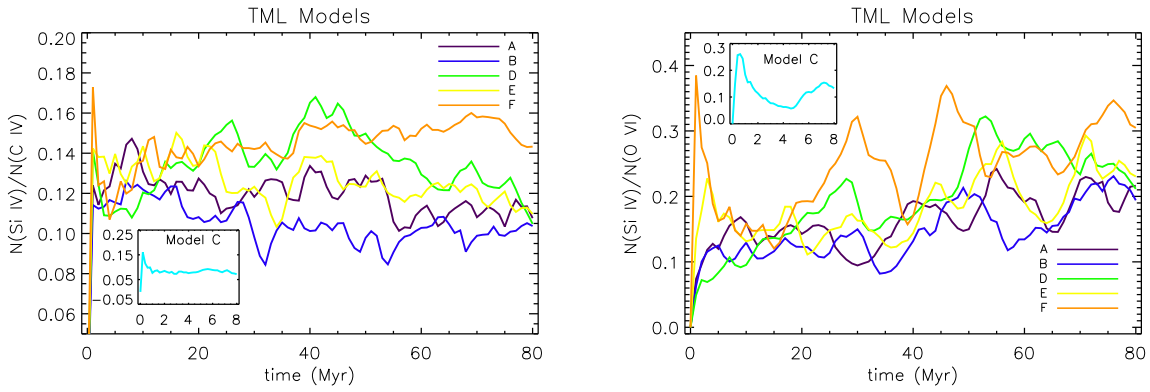

Fig. 3.— Left and right panels, respectively, show N(Si IV)/N(C IV) and N(Si IV)/N(O VI) as a function of time from the TML models. These ratios were calculated from column density averages that, themselves were calculated from large numbers of vertical sightlines through the domain (256 sightlines for Models A, B, D, E, and F and 512 sightlines for Model B). The inset is for Model C, which ran to t=8 Myr.

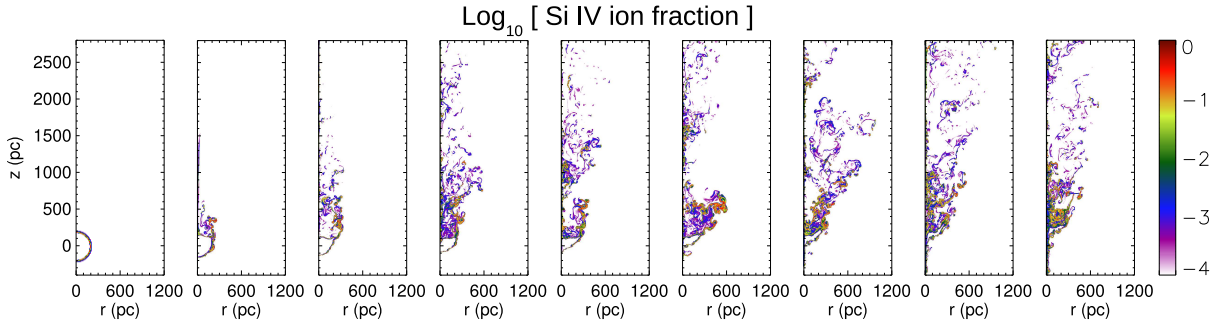

Fig. 4.— Si IV ion fraction from HVC Model B with logarithmic color scale. From left to right, each panel is plotted at 15 Myr intervals from $t = 0$ to $t = 120$ Myr. The simulations were carried out in 2D cylindrical coordinates, and only half of the spherical cloud is shown along a plane that cuts through the center of the cloud.

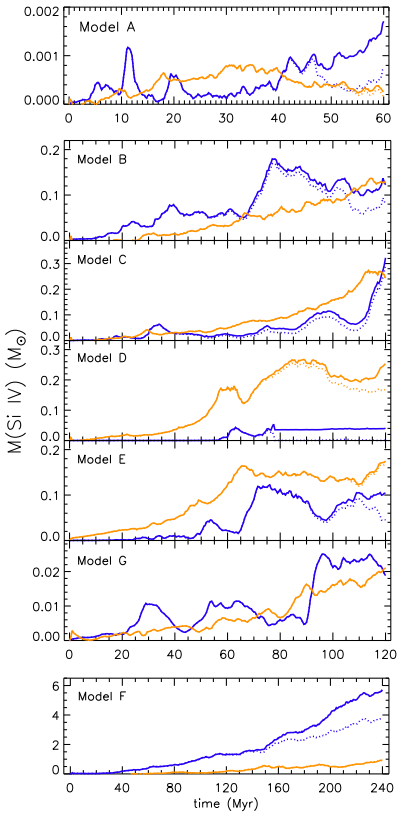

Fig. 5.— Mass (in solar masses) of Si IV as a function of time from seven HVC models. In each panel, the blue and orange lines correspond to the masses of low- and high-velocity Si IV, respectively. The dotted lines trace the Si IV masses that are in the domain as a function of time while the solid lines track the sum of the mass of Si IV ions that are in the domain plus the mass of Si IV ions that have escaped from the domain by flowing through the upper boundary of the domain. In most panels, the orange dotted lines are overlapped by the orange solid lines and so are not readily apparent.

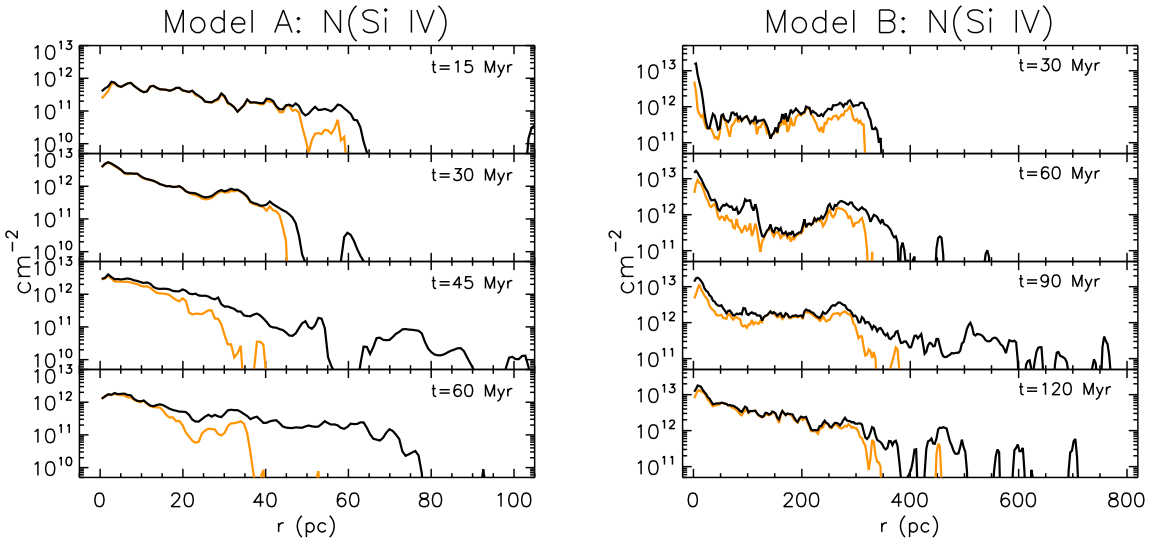

Fig. 6.— N(Si IV) as a function of off-axis radius (i.e., distance from the center of the cloud) for HVC Model A (left) and HVC Model B (right) at four different epochs (at t= 15, 30, 45, and 60 Myr for HVC Model A and at t=30, 60, 90, 120 for HVC Model B). Note that the initial radii of HVC Model A and HVC Model B are approximately 20 pc and 150 pc, respectively, and that t=15 Myr in Model A corresponds to a similar evolutionary phase as t=60 Myr in Model B. The orange lines track the column densities of the high-velocity material while the black lines track the column densities irrespective of velocity.

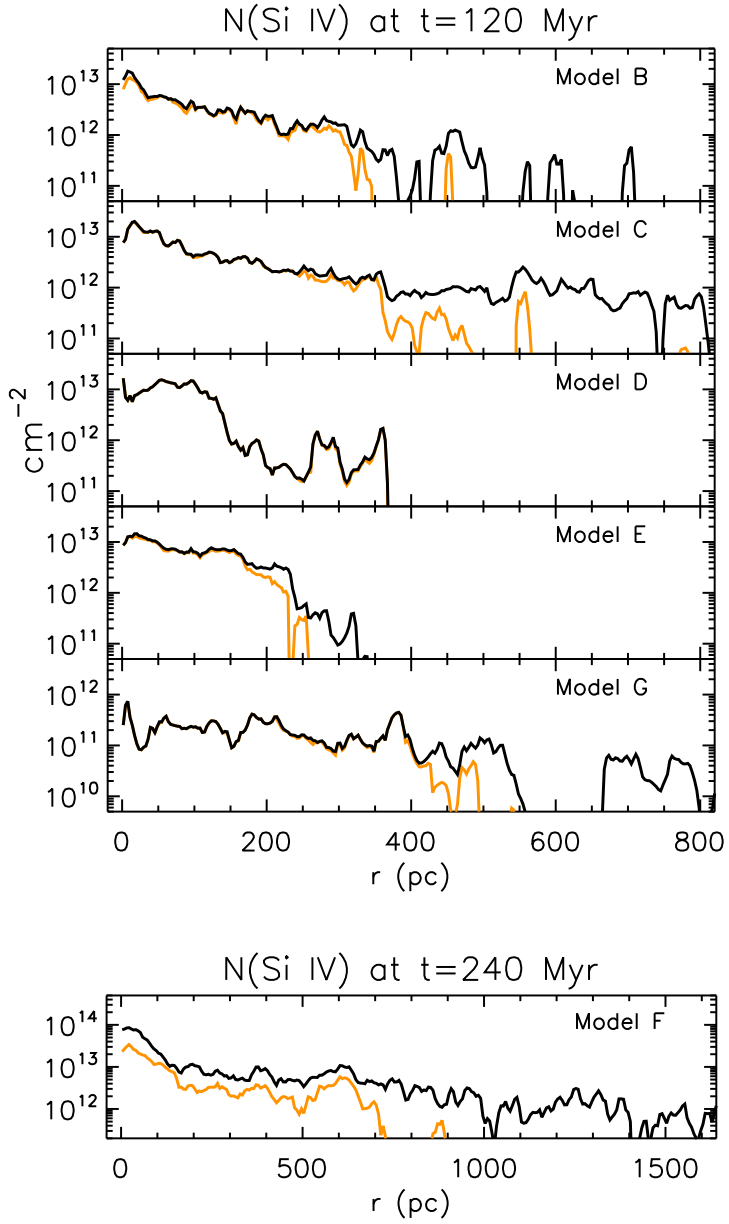

Fig. 7.— N(Si IV) as a function of off-axis radius (i.e., distance from the center of the cloud) for our HVC Models (from top to bottom, HVC Model B, C, D, E, G, and F) at the last epochs of the simulations (i.e., at t=120 Myr for HVC Models B, C, D, E, and G and at t=240 Myr for HVC Model F). The orange lines show the column densities of the high-velocity material while the black lines show the total column densities, i.e., the column densities irrespective of velocity.

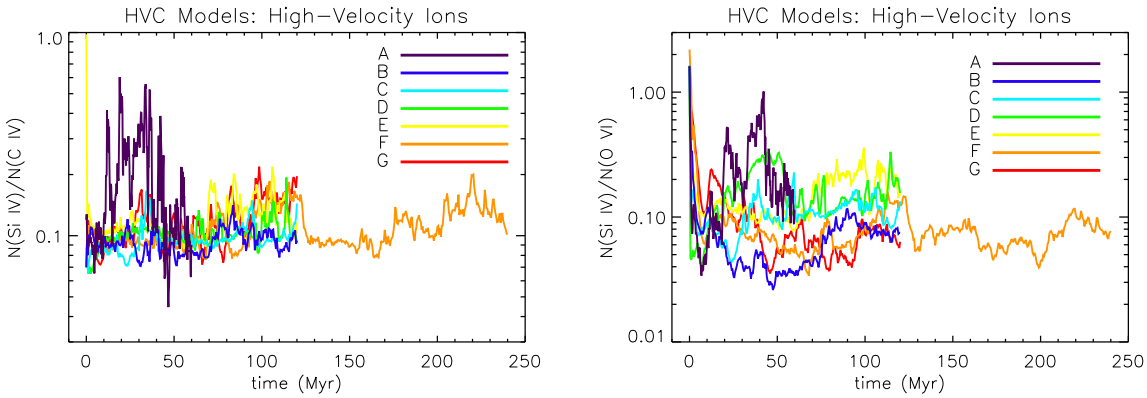

Fig. 8.— High-velocity N(Si IV)/N(C IV) and N(Si IV)/N(O VI) as functions of time from the HVC models in the left and right panel, respectively. As for Figure 3, the ratios were calculated from the averages of column densities that were, themselves calculated for many vertical sightlines through the domain. While averaging over these sightlines, we included only the sightlines along which the column density of the relevant high-velocity ion was above a cut-off column density (10^{11} cm^{-2} for HVC Models B, C, D, E, and F and 10^{10} cm^{-2} for HVC Models A and G).

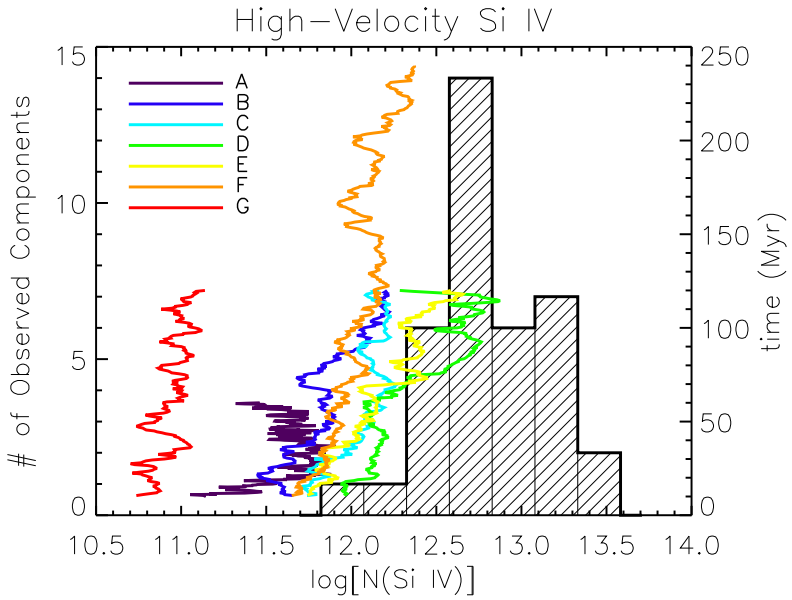

Fig. 9.— Column densities of high-velocity Si IV: comparison between observations and predictions from our HVC models. The gray histogram presents 37 detected components of high-velocity Si IV column densities obtained from Table 2 of Shull et al. (2009). The number of observed components (in the left y-axis) within a range of logarithmic column densities of high-velocity Si IV (in the x-axis) is plotted. The time evolution (from $t = 10$ Myr) of average column densities of high-velocity Si IV predicted from our seven HVC models is shown as solid color lines (the right y-axis versus x-axis). The average column density of high-velocity Si IV at each epoch is calculated according to equations (2) and (3) in KHS11 with the same cut-off ($N_{cut} = 10^{11}$ cm^{-2} for HVC Models B through F and 10^{10} cm^{-2} for HVC Models A and G).

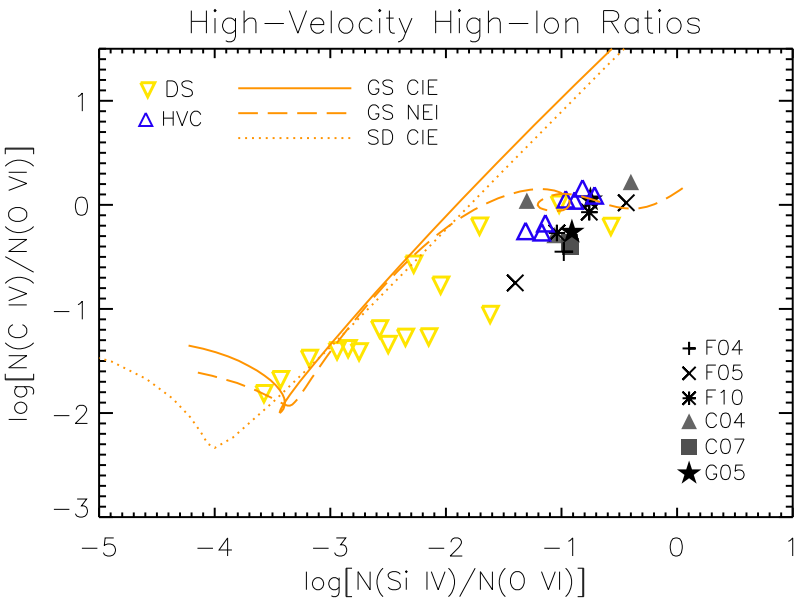

Fig. 10.— N(Si IV)/N(O VI) versus N(C IV)/N(O VI) in logarithmic scale: comparison between predictions from various models and observations for high-velocity ions. Model predictions are presented with colored symbols and lines (whose labels are shown on the upper-left corner) and observations are displayed with black and gray symbols (whose labels are shown on the lower-right corner). Predictions are from the following models: shock heating from Dopita & Sutherland (1996, DS: yellow upside-down triangles from their Tables 2A, 2B, 2C, and 2D), our HVC models from high-velocity high-ions (blue triangles from mean values in Table 4), and radiative cooling model of hot gas from Gnat & Sternberg (2007, their collisional ionization equilibrium predictions are from their Table 2A, denoted by GS CIE, and traced by a solid orange line, and their isochoric non-equilibrium ionization model predictions are from their Table 2B, denoted by GS NEI, and traced by a dashed orange line) and Sutherland & Dopita (1993, their collisional ionization equilibrium predictions are from their Table 5, denoted by SD CIE, and traced by a dotted orange line). Note that the models indicated by orange lines are more relevant to the low-velocity results shown in Figure 12, but we include these models here for convenient comparison between the low- and high-velocity results. Note again that before presenting any of these model predictions, we have converted the assumed abundances to those of Wilms et al. (2000). Observations are from the following references: Fox et al. (2004, F04: + symbols from their Table 4 including the results of detected ion column densities only), Fox et al. (2005, F05: × symbols from their Table 5 including the results of detected ion column densities only), Fox et al. (2010, F10: ∗ symbols from their Tables 1 and 2 including the results of detected ion column densities only), Collins et al. (2004, C04: gray filled triangles from their Tables 2 and 4 including the results of detected ion column densities only), Collins et al. (2007, C07: gray filled squares from their Tables 4 and 7 including the results of strong line only of the doublet), and Ganguly et al. (2005, G05: dark filled stars from their Table 5 including the high-velocity results only, i.e., $v_{LSR} \approx +100$ and $+184$ km s^{-1}).

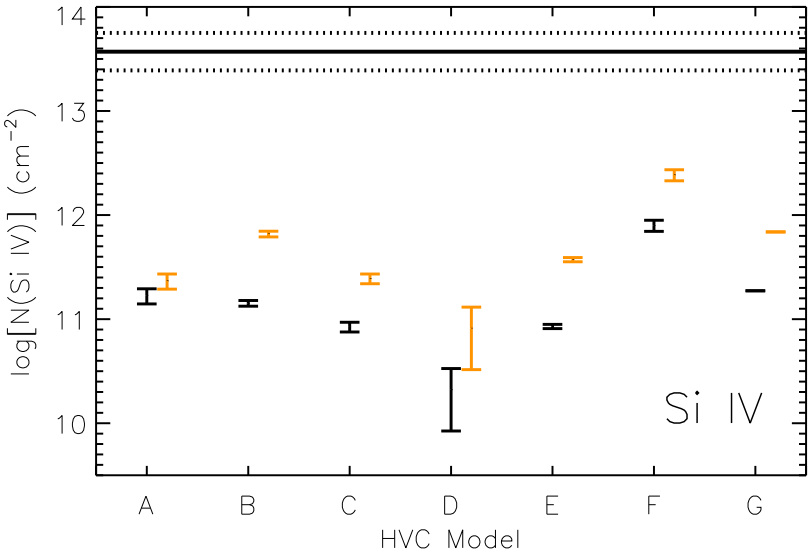

Fig. 11.— Comparison between the average low-velocity Si IV column density observed on halo sightlines and the predicted average for the halo that results from a population of model HVCs. The predicted values from each model are indicated by bars. The black bars are predicted column densities that were obtained from the mass integrations to the ends of simulations (columns [2] and [3] in Table 5) and the orange bars are the predicted column densities that effectively include the mass integrations between the ends of the simulations and the ends of the clouds' lifetimes (columns [5] and [6] in Table 5). The top and bottom ends correspond to 'Domain+Escaped' and 'Domain only', respectively, in Table 5. The column densities shown in this figure were calculated with an HVC infall rate $\dot{\mathcal{M}}^{\rm H}_{\rm HVC} = 0.5 M_\odot$ yr^{-1} as in Table 5. When the infall rate increases to a factor 2 larger value $\dot{\mathcal{M}}^{\rm H}_{\rm HVC} = 1.0 M_\odot$ yr^{-1}, the column densities also increase by a factor of 2, i.e., both black and orange bars are shifted upwards by a factor of 2. The observed values are from Wakker et al. (2012). The average of integrated column densities of Si IV along the 32 extra-galactic sightlines from their Figure 6 (top panel for the case of Si IV) is indicated by the horizontal solid line and its error ranges are shown as dotted lines.

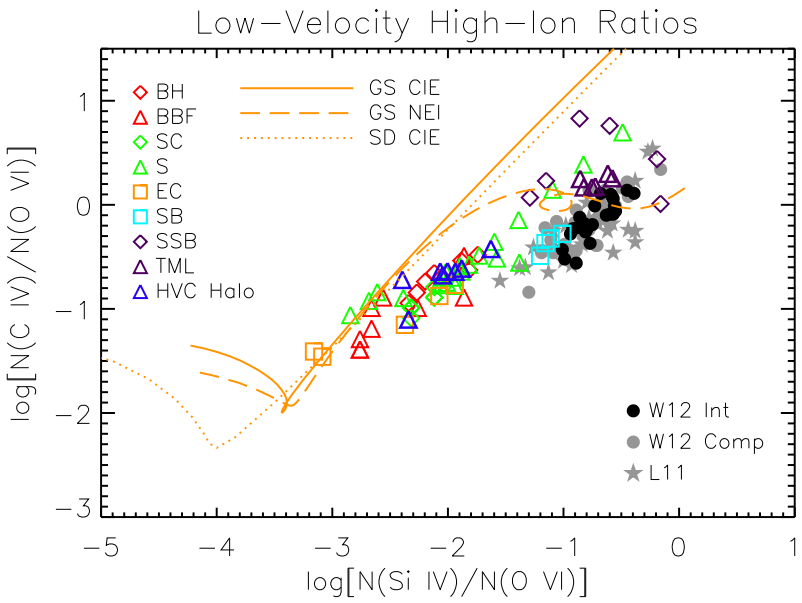

Fig. 12.— N(Si IV)/N(O VI) versus N(C IV)/N(O VI) in logarithmic scale: comparison between predictions from various models and observations for low-velocity ions. Model predictions are presented with colored symbols and lines whose labels are on the upper-left corner and observations are displayed with black and gray symbols whose labels are on the lower-right corner. Predictions are from the following models: thermal conduction from Boehringer & Hartquist (1987, BH: red diamonds from their Table 2) and Borkowski et al. (1990, BBF: red triangles estimated from their Figure 6), supernova remnants from Slavin & Cox (1992, SC: green diamonds estimated from their Figure 7) and Shelton (2006, S: green triangles obtained from the results at 22 epochs of simulation number 103), radiative cooling of hot gas from Edgar & Chevalier (1986, EC: orange squares from their Table 1), Gnat & Sternberg (2007, their collisional ionization equilibrium predictions are from their Table 2A, denoted by GS CIE, and traced by a solid orange line, and their isochoric non-equilibrium ionization model predictions are from their Table 2B, denoted by GS NEI, and traced by a dashed orange line), and Sutherland & Dopita (1993, their collisional ionization equilibrium predictions are from their Table 5, denoted by SD CIE, and traced by a dotted orange line), galactic fountains from Shapiro & Benjamin (1993, SB: cyan squares from their Table 1), and turbulent mixing from Slavin et al. (1993, SSB: purple diamonds from their Table 4A) and our TML models (TML: purple triangles from mean values in Table 3). Ratios of low-velocity high ions predicted from our HVC models are represented by blue triangles (HVC Halo). These ratios are calculated from Table 2 of HKS12, where average column densities of C IV and O VI were presented, and Table 5. Among four average column densities in these tables, we take only two of the column densities that include the effect of the cloud's lifetime evolution. The ratios are calculated after taking the average of the two β-corrected column densities of 'Domain only' and 'Domain + Escaped'. Note that before presenting any of these model predictions, we have converted the assumed abundances to those of Wilms et al. (2000). Observations are from the following references. Dark and gray filled circles are ratios of integrated and component column column densities, respectively, from Wakker et al. (2012). From their Table 2, we extracted 24 ratios of integrated column densities and 41 ratios of component column densities only for the detected cases. Gray filled stars are from Lehner et al. (2011) who observed column densities of low-velocity high ions along sightlines to 38 stars in the Milky Way disk. From their Table 4, we extracted 29 ratios of detected column densities.

Table 1. TML Models

	Domain		Hot Gas			Initial Interface	Cool Gas		
Model	x (pc)	y (pc)	n_H (cm^{-3})	T (K)	v_x (km s^{-1})	$y = f(x)$	n_H (cm^{-3})	T (K)	v_x (km s^{-1})
TML A [a]	[0, 100]	[-250, 50]	10^{-4}	10^6	0	$y = (2.5\text{pc})\ \sin(\frac{2\pi x}{100\text{pc}})$	0.1	10^3	100
TML B [b]	[0, 100]	[-250, 50]	10^{-4}	10^6	0	$y = (2.5\text{pc})\ \sin(\frac{2\pi x}{100\text{pc}})$	0.1	10^3	100
TML C	[0, 10] [c]	[-25, 5]	10^{-4}	10^6	0	$y = (0.25\text{pc})\ \sin(\frac{2\pi x}{10\text{pc}})$	0.1	10^3	100
TML D	[0, 100]	[-250, 50]	10^{-4}	10^6	0	$y = (2.5\text{pc})\ \sin(\frac{2\pi x}{100\text{pc}})$	0.1	10^3	50 [d]
TML E	[0, 100]	[-250, 50]	10^{-4}	10^6	0	$y = (5.0\text{pc})\ \sin(\frac{2\pi x}{100\text{pc}})$ [e]	0.1	10^3	100
TML F	[0, 100]	[-250, 50]	$\frac{1}{3} \times 10^{-4}$	3×10^6 [f]	0	$y = (2.5\text{pc})\ \sin(\frac{2\pi x}{100\text{pc}})$	0.1	10^3	100

Note. — Model parameters for TML simulations. This table is reproduced from Table 1 of KS10.

[a]Reference TML simulation

[b]TML B is a higher spatial resolution model by a factor of 2 than TML A.

[c]The computational domain is 1/10 of TML A.

[d]Cool gas has half initial speed of TML A.

[e]Amplitude of initial interface between hot and cool gas is twice that of TML A.

[f]The temperature of the hot gas is three times larger than TML A.

Table 2. HVC Models

	Domain		Ambient Medium		Cloud				
Model	r (pc)	z (pc)	n_H (cm^{-3})	T (K)	Radius [a] (pc)	$v_{z,cl}$ [b] km s^{-1}	$n_{H,ctr}$ [c] cm^{-3}	$M_{init,T}$ [d] $M_\odot$	$M_{init,v}$ [e] $M_\odot$
HVC A	[0,300]	[-200,600]	1.0×10^{-4}	10^6	20	-100	0.1	120	130
HVC B	[0,1200]	[-400,2800]	1.0×10^{-4}	10^6	150	-100	0.1	4.9×10^4	5.1×10^4
HVC C	[0,1200]	[-400,2800]	1.0×10^{-4}	10^6	150	-150	0.1	4.9×10^4	5.1×10^4
HVC D	[0,1200]	[-400,4400]	1.0×10^{-4}	10^6	150	-300	0.1	4.9×10^4	5.1×10^4
HVC E	[0,1200]	[-400,2800]	1.0×10^{-4}	10^6	150	-150	0.1	4.9×10^4	4.9×10^4
HVC F	[0,2400]	[-800,8800]	1.0×10^{-4}	10^6	300	-100	0.1	4.0×10^5	4.2×10^5
HVC G	[0,1200]	[-400,2800]	1.0×10^{-5}	10^6	150	-100	0.01	4.9×10^3	5.1×10^3

Note. — Model parameters for HVC simulations. This table is reproduced from Table 1 of KHS11 with additional information on the domain size.

[a]Approximate radius of the model cloud in HVC simulations except HVC E, which is a uniform density cloud with an exact radius. The HVC model clouds have radial density profiles. See Figure 1 of KHS11 for the detailed density profile of each HVC model cloud.

[b]Initial velocity of the cloud along the z-direction measured in the observer's frame.

[c]Initial hydrogen number density of the cloud at its center. Note that inially all the HVC models have the same cloud temperatures at cloud centers ($T = 10^3$ K) and their radial temperature profiles are determined by the cloud density profiles with the condition that the initial pressure is the same in the entire region throughout both the cloud and the ambient medium.

[d]Initial mass of cloud having a temperature $T < 10^4$ K.

[e]Initial mass of cloud moving with $v_{z,cl}$. Note that all cloud material with a hydrogen number density greater than 5 times the ambient medium's hydrogen number density moves initially at speed $v_{z,cl}$ relative to the ambient medium.

Table 3. Column Density Ratios from TML Models

Model	N(Si IV) / N(C IV)				N(Si IV) / N(O VI)			
	mean	median	σ [a]	[min, max]	mean	median	σ [a]	[min, max]
TML A [b]	0.12	0.12	0.0081	[0.10, 0.13]	0.17	0.18	0.038	[0.094, 0.24]
TML B [b]	0.10	0.10	0.0063	[0.084, 0.12]	0.16	0.15	0.040	[0.082, 0.23]
TML C [c]	0.082	0.082	0.0056	[0.072, 0.089]	0.14	0.14	0.012	[0.12, 0.15]
TML D [d]	0.14	0.14	0.015	[0.10, 0.17]	0.23	0.24	0.050	[0.15, 0.32]
TML E [b]	0.12	0.12	0.0088	[0.10, 0.14]	0.19	0.19	0.048	[0.11, 0.29]
TML F [b]	0.15	0.15	0.0063	[0.13, 0.16]	0.27	0.26	0.049	[0.16, 0.37]

[a]standard deviation

[b]averaged over $t \in [20, 80]$ Myr

[c]averaged over $t \in [6, 8]$ Myr

[d]averaged over $t \in [30, 80]$ Myr

Table 4. Column Density Ratios from HVC Models

Model	N(Si IV) / N(C IV)				N(Si IV) / N(O VI)			
	mean	median	σ [a]	[min, max]	mean	median	σ [a]	[min, max]
HVC A [b]	0.20	0.16	0.12	[0.045, 0.60]	0.26	0.19	0.18	[0.056, 1.0]
HVC B [c]	0.094	0.092	0.013	[0.071, 0.14]	0.059	0.049	0.023	[0.026, 0.12]
HVC C [c]	0.099	0.096	0.016	[0.071, 0.17]	0.11	0.11	0.030	[0.043, 0.23]
HVC D [c]	0.11	0.10	0.013	[0.082, 0.19]	0.17	0.15	0.065	[0.093, 0.35]
HVC E [c]	0.12	0.11	0.027	[0.086, 0.22]	0.16	0.13	0.061	[0.078, 0.36]
HVC F [d]	0.11	0.10	0.025	[0.076, 0.20]	0.075	0.072	0.022	[0.034, 0.16]
HVC G [c]	0.12	0.12	0.030	[0.072, 0.22]	0.071	0.068	0.024	[0.035, 0.15]

[a]standard deviation

[b]calculated over a range of $t \in [10, 60]$ Myr

[c]calculated over a range of $t \in [20, 120]$ Myr

[d]calculated over a range of $t \in [20, 240]$ Myr

Table 5. Average Column Density of Low-Velocity Si IV in the Halo from HVC Simulations

	Average N(Si IV) during the simulations[a] (10^{11} cm^{-2})			Average N(Si IV) during the cloud's lifetime[b] (10^{11} cm^{-2})	
Model	Domain only[c]	Domain + Escaped[d]	β_{HVC}[e]	Domain only[c]	Domain + Escaped[d]
(1)	(2)	(3)	(4)	(5)	(6)
HVC A	1.4	2.0	0.721	1.9	2.7
HVC B	1.3	1.5	0.216	6.2	7.0
HVC C	0.75	0.93	0.344	2.2	2.7
HVC D	0.084	0.34	0.257	0.33	1.3
HVC E	0.81	0.89	0.228	3.6	3.9
HVC F	7.0	8.9	0.327	21	27
HVC G	1.9	1.9	0.272	6.9	6.9

Note. — The column densities presented in this table are calculated with the same HVC infall rate $\dot{\mathcal{M}}^{\rm H}_{\rm HVC} = 0.5 M_\odot$ yr^{-1} as in HKS12. When the infall rate increases to a factor 2 larger value $\dot{\mathcal{M}}^{\rm H}_{\rm HVC} = 1.0 M_\odot$ yr^{-1}, the column densities also increase by a factor of 2.

[a]Average N(Si IV) in the halo due to low-velocity Si IV produced during the simulation times: 60 Myrs for HVC Model A, 120 Myrs for HVC Models B, C, D, E, and G, and 240 Myrs for HVC Model F

[b]Average N(Si IV) in the halo due to low-velocity Si IV produced throughout the cloud's lifetime. The column densities in columns (5) and (6) are obtained by dividing the column densities in columns (2) and (3) by β_{HVC} in column (4), respectively, in order to account for the contributions made by ions after the simulations terminated.

[c]Column densities are calculated from Si IV ions that are counted in the simulation domain.

[d]Column densities are calculated from Si IV ions in the simulation domain plus Si IV ions that have escaped through the top boundary of the simulation domain.

[e]The fraction of the original HVC H I mass that has been 'removed' due to either ablation or ionization by the end of the simulation.

Table 6. Composite Model of Low-Velocity High Ions in the Milky Way's Halo

	Si IV	C IV	N V	O VI
Observed[a] (10^{13} cm^{-2})	2.9	11.3	2.5	16.2
(1) HVCs[b]	2%	12%	22%	35%
	(5%)	(23%)	(44%)	(70%)
(2) Extraplanar SNRs[c]	...	4%	8%	10%
(3) Galactic fountains[d]	$19-30\%$	$26-41\%$	$20-30\%$	55%
	$(7-11\%)$	$(10-15\%)$	$(7-11\%)$	(20%)
(4) Photoionization by external radiation field[e]	11%	25%	...	...
Total	$32-43\%$	$67-82\%$	$50-60\%$	100%[f]
	$(23-27\%)$	$(62-67\%)$	$(59-63\%)$	(100%)[f]

Note. — Each model component's contribution is expressed as a percentage of the observed column density of Si IV, C IV, N V, and O VI. The main values are estimated using the same HVC infall rate $\dot{\mathcal{M}}^{\rm H}_{\rm HVC} = 0.5 M_\odot$ yr^{-1} as in HKS12, while the values in the parentheses (in the third, sixth, and last rows) are estimated with a factor 2 larger infall rate of HVCs, i.e., $\dot{\mathcal{M}}^{\rm H}_{\rm HVC} = 1.0 M_\odot$ yr^{-1} in Equation (1). See the text for more details.

[a]Average observed column densities with latitude correction ($N \sin|b|$) calculated from Table 2 of Wakker et al. (2012). Only the integrated column densities along the detected sightlines are included. The O VI value is obtained after removing contribution from the Local Bubble ($\sim 7 \times 10^{12}$ cm^{-2}, Oegerle et al. 2005). Note that these new values are slight larger than those in Table 3 of HKS12 for Si IV, C IV, and O VI, while the N V value is the same within errors.

[b]From our HVC Model B (reference model); the average of the 'Domain-only' and 'Domain+Escaped' column densities that were calculated taking into account the lifetime evolution of the model cloud (e.g., for Si IV, the average of column (5) and column (6) for HVC B in Table 5).

[c]From the model with case 1 and drag coefficient 1 in Table 8 of Shelton (2006). The column densities were re-calculated according to the abundance adjustment from Grevesse & Anders (1989, used in Shelton) to Wilms et al. (2000).

[d]From Table 1 of Shapiro & Benjamin (1993). The column densities were first re-calculated in order to adjust the abundances from Allen (1973, used in Shapiro & Benjamin) to Wilms et al. (2000), and then rescaled by a factor of 0.37 to 0.60 so that the composite model would explain all of the observed O VI.

[e]From Figures 3(a) and 3(b) in Ito & Ikeuchi (1988). We assume that negligible N V and O VI is produced due to photoionization in their model. Again, the column densities of Si IV and C IV were re-calculated using the abundances of Wilms et al. (2000). (We assumed that the cosmic abundances mentioned in Ito & Ikeuchi (1988) are the abundances of Allen (1973).)

[f]By design, our composite model reproduces 100% of the O VI.